A 7-Yr Climatology of the Initiation, Decay, and Morphology of Severe Convective Storms during the Warm Season over North China

RUOYUN MA,[a,b] JIANHUA SUN,[a,b,c] AND XINLIN YANG[d]

[a] *Key Laboratory of Cloud-Precipitation Physics and Severe Storms (LACS), Institute of Atmospheric Physics, Chinese Academy of Sciences, Beijing, China*
[b] *University of Chinese Academy of Sciences, Beijing, China*
[c] *Southern Marine Science and Engineering Guangdong Laboratory (Zhuhai), Zhuhai, China*
[d] *Key Laboratory of Regional Climate-Environment for Temperate East Asia (RCE-TEA), Institute of Atmospheric Physics, Chinese Academy of Sciences, Beijing, China*

(Manuscript received 16 March 2020, in final form 7 May 2021)

ABSTRACT: The present work established a 7-yr climatology of the initiation, decay, and morphology of severe convective storms (SCSs) during the warm seasons (May–September) of 2011–18 (except 2014) over North China. This was achieved by using severe weather reports, precipitation observations, and composite Doppler radar reflectivity data. A total of 371 SCSs were identified. SCSs primarily initiated around noon with the highest frequency over the high terrain of Mount Taihang, and they mostly decayed over the plains at night. The storm morphologies were classified into three types of cellular storms (individual cells, clusters of cells, and broken lines), six types of linear systems (convective lines with no stratiform, with trailing stratiform, leading stratiform, parallel stratiform, embedded lines, and bow echoes), and nonlinear systems. Three types of severe convective weather, namely, short-duration heavy rainfall, hail, and thunderstorm high winds, associated with these morphologies were investigated. A total of 1429 morphology samples from the 371 SCSs were found to be responsible for 15 966 severe convective weather reports. Nonlinear systems were the most frequent morphology, followed by clusters of cells. Convective lines with trailing stratiform were the most frequent linear morphology. Linear (nonlinear) systems produced the most short-duration heavy rainfall (hail and thunderstorm high wind) reports. Bow echoes were most efficient in producing both short-duration heavy rainfall and thunderstorm high wind reports whereas broken lines had the highest efficiency for hail production. The results in the present study are helpful for local forecasters to better anticipate the storm types and associated hazardous weather.

KEYWORDS: Severe storms; Climatology

1. Introduction

Severe convective weather (SCW), such as short-duration heavy rainfall (SDHR), thunderstorm high winds (THWs), and hail, occurs frequently over North China (J. Chen et al. 2013a; Yang et al. 2017; Li et al. 2018) and poses a great threat to life and property in this region. Accurate forecasting of severe convective storms (SCSs) over North China is particularly challenging, as storm initiation and evolution over this region are influenced greatly by the complex underlying surfaces, which include the Bohai Sea, Yanshan Mountains, and Taihang Mountains, and megacity Beijing (Sun et al. 2006; Sun and Yang 2008; Chen et al. 2011; Chen et al. 2012; Zhang and Cui 2012; Xiao et al. 2013, 2015; Li et al. 2017). Improved forecasting requires better understanding of the initiation and organization of SCSs, as well as the frequency of various storm morphologies and their relations with different types of SCW.

Convection initiation statistics over complex terrain have been extensively studied worldwide (Kuo and Orville 1973; Karr and Wooten 1976; Purdom 1976; Banta and Schaaf 1987; Schaaf et al. 1988; Banta 1990; Kovacs and Kirshbaum 2016). Over North China, greater emphasis has been put on convection initiation mechanisms through case studies (e.g., Fan et al. 2009; M. X. Chen et al. 2013; Liu et al. 2015; Li et al. 2017; Qin and Chen 2017; Xia and Zhang 2019; Hua et al. 2020), and the climatology of convection initiation is less studied. One climatology study (Chen et al. 2012), for example, showed that convective storms frequently initiated over the northwestern mountains in the afternoon as a result of solar heating while convection tended to initiate over the southeastern plains at night. However, previous climatological studies rarely focused solely on convection that eventually produced SCW in this region.

Classification of storm morphology is important because different morphologies are reflective of different dynamics dominating the storm and tend to produce different types of SCW. Bluestein and Jain (1985) developed a taxonomy for severe squall lines occurring in Oklahoma, which comprised broken line, back building, broken areal, and embedded areal. Parker and Johnson (2000) identified three morphologies for linear convective systems: convective lines with trailing (TS), leading (LS), and parallel stratiform (PS) precipitation. Two patterns of organization (i.e., training-line-adjoining stratiform and back-building) for extreme-rain-producing mesoscale convective systems (MCSs) were further proposed by

Supplemental information related to this paper is available at the Journals Online website: https://doi.org/10.1175/MWR-D-20-0087.s1.

Corresponding author: Jianhua Sun, sjh@mail.iap.ac.cn

DOI: 10.1175/MWR-D-20-0087.1

Schumacher and Johnson (2005). Gallus et al. (2008, hereafter G08) classified warm-season convective storms over the central United States into nine morphologies and analyzed the severe weather reports associated with each morphology. Following the classification scheme in G08, Lombardo and Colle (2010) investigated the spatial and temporal distribution of organized convective structures over the northeastern United States. Lombardo and Colle (2011, hereafter LC11) further studied the storm structures associated with severe weather over that region. They found that cellular structures were the primary hail producers while tornadoes developed mainly from cellular and linear structures. Over the coastal zone of the northeastern United States, THWs and hail were produced primarily by cellular and linear storms, while tornadoes were equally likely from cellular, nonlinear and linear structures.

Similar studies have also been carried out in China, though the focus was mainly over central east China. For example, Meng et al. (2013) examined the formation mode, organizational mode, and dissipation mode of squall lines over east China. Their results indicated that squall lines commonly formed in a broken-line mode, displayed a trailing-stratiform mode, and dissipated in a reversed broken-line mode. Zheng et al. (2013, hereafter Z13) performed a comprehensive study of the organizational modes of MCSs and associated SCW over central east China. They found that bow echoes (BEs) generated the most SCW reports on average while most TS systems were attendant with SDHR and THWs. Embedded line (EL) and PS systems were most frequently associated with extreme SDHR. Wang et al. (2014) classified the organizational modes of MCSs during the mei-yu season over the Yangtze River basin into nonlinear and eight linear types. It is demonstrated that linear-mode MCSs tended to develop in the vicinity of the Yangtze River, especially over low-lying areas and river valleys. Six of the linear modes had been identified in previous studies, but two modes (embedded line and long line MCSs) were identified for the first time in their study. By contrast, research on the storm morphology classification and associated SCW over North China have received much less attention. Yang and Sun (2018) examined the storm morphologies responsible for THWs over North China. They found that THWs over the mountains and plains were caused primarily by clusters of cells and linear systems, respectively.

Owing to the differences in synoptic weather pattern and underlying surface conditions, the convective storm characteristics vary greatly from region to region (Liang et al. 2012; J. Chen et al. 2013b; Yang et al. 2019; Meng et al. 2021). Therefore, investigation of local storm statistics is necessary. However, a climatology that details the spatiotemporal distribution of the initiation and decay of SCSs over North China is lacking. In addition, little is known in this region regarding the characteristics of storm morphology and associated SCW. Therefore, the present study attempts to address the following questions: What are the general characteristics (e.g., initiation, decay, and lifetime) of SCSs over North China? What is the occurrence frequency of various storm morphologies and their relations with different types of SCW? And how do the statistics over North China compare to those in other regions of the world? The remainder of this paper is organized as follows. Section 2 introduces data and methodology. Section 3 presents statistical results, including spatiotemporal distribution of the initiation and decay of SCSs, and classification of storm morphology and their relations with SCW of different types and severities. Section 4 outlines the conclusions of this study.

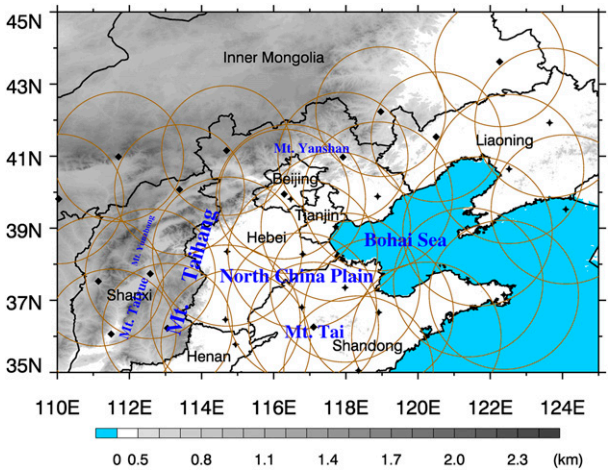

FIG. 1. Topographic map (shading; units: km) with names of cities/provinces and major landforms over North China. A total of 32 operational radars including 18 S-bands (stars) and 14 C-bands (diamonds) over this region are marked. The circles centered at the radars have radii of 230 km (S-bands) or 200 km (C-bands).

2. Data and methodology

a. Data source

In this study, the North China region was defined as the region covering 35°–45°N, 110°–125°E (Fig. 1). The mosaics of composite Doppler radar reflectivity with 0.01° × 0.01° and 6–10-min resolution, 3-hourly severe weather reports (SWRs), and hourly precipitation observations during the warm seasons (May–September) of 2011–18 (except for 2014) over North China were used. Year 2014 was excluded because radar data availability was notably lower in this year (81%) compared with other years (> 93%). According to the National Meteorological Center, China Meteorological Administration (CMA), SCW refers to SDHR with hourly precipitation ≥ 20 mm h^{-1}, THWs with wind speeds ≥ Beaufort scale 8 (or 17.2 m s^{-1}), hail with diameters ≥ 5 mm, and any tornado (Zheng et al. 2015). Tornadoes were not considered in this study due to their relatively infrequent occurrence over North China (Fan and Yu 2015).

The THW and hail events were obtained from the SWRs dataset. The SWRs had a time interval of 3 h, namely, there were eight files per day. In each file, all severe weather events that occurred in the 3-h period were recorded with station ID, location (longitude and latitude), time (hour and minute), weather phenomena and other information. For example, a SWR file at 0200 Beijing Standard Time (BST; BST = UTC + 8 h) recorded all severe weather that occurred from 0000 to 0259 BST. Severe weather including thunder, high winds, hail, tornadoes,

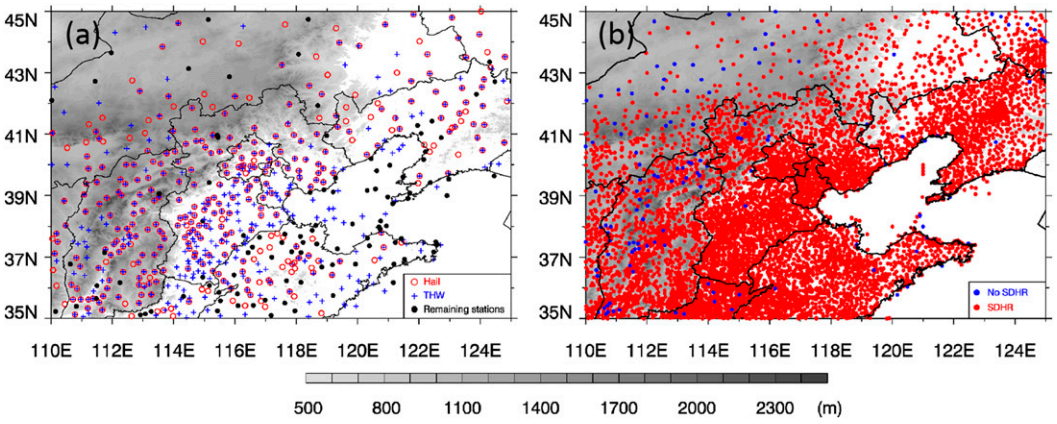

FIG. 2. Spatial distribution of stations in (a) SWRs and (b) surface precipitation observations used in this study. Gray shading represents topography. In (a), the red open circles, blue plus signs, and black dots indicate stations with at least one occurrence of hail, at least one occurrence of THWs, and with zero occurrence of hail and THWs, during the study period, respectively. In (b), the red and blue dots indicate stations with at least one or with zero occurrence of SDHR during the study period, respectively.

snow, glaze, and those that caused obstruction to visibility such as floating dust, sand storms, fog, and haze, were recorded if they met the criteria of CMA. The wind speed and direction were provided for a high wind report, and the maximum hail diameter was provided for a hail report.

During our study period, the SWRs were available at 97% of the time (i.e., 97% of the study period had a SWR file), recording a total of 633 stations over North China which had at least one occurrence of the aforementioned severe weather. The high wind reports in the SWRs included not only convectively generated ones, but also a variety of nonconvective winds such as those related with cold air and those caused by topography. Since we were interested only in those caused by deep moist convection, the method described in Yang et al. (2017) was employed to select THWs from all high wind reports using cloud-to-ground lightning data. According to the CMA, a new report is required if the magnitude of the wind speed is reinforced or a mistake is found in a previous report. Therefore, there might be multiple reports within one SWR file for the same wind event. When this was the case, the latest report was retained and the previous one(s) were removed. This was also implemented for hail reports. After all these filters were applied, a total of 457 (72.2% of the 633 stations) and 348 (55.0% of the 633 stations) stations in the SWR dataset over North China were retained, which had at least one occurrence of THWs and hail, respectively, during our study period and domain (Fig. 2a).

The SDHR reports were obtained from surface precipitation observations. The data had a time interval of 1 h and were available at 99.7% of the time during the study period. Owing to the continual construction of surface weather stations, there was a general increase in the number of precipitation stations during the study period. This could be problematic for the identification of SCSs because the assessment of storm severity was based on the number of surface stations recording SCW reports (see the definition of SCSs in section 2b). Therefore, we used the same 7042 precipitation stations in 2011 over North China for relevant analyses (Fig. 2b). It should be noted that underreporting of SCW existed because these observations were based on point measurements, and those that did not occur at the observation stations were not reported. Also, the observations were unavoidably influenced by the spatial inhomogeneity of the station distribution. These problems are also present in the National Climatic Data Center's Storm Events Database, as have been noticed by a number of studies (Weiss and Bluestein 2002; G08; Duda and Gallus 2010; Smith et al. 2012). In addition, composite radar reflectivity data from 32 Doppler radars in North China were used to examine storm initiation, organization and decay. The radar data had a nominal availability of 96.4% during the study period, and was available every 10 (6) min before (after) 1440 BST, 14 Jun 2016 at approximately $0.01° \times 0.01°$ grid spacing.

After the three types of SCW were obtained, they were each divided into two severity groups to explore the distribution of storm morphologies among SCW with different severities. SDHR reports were divided into ordinary SDHR ($20 \leq$ hourly rainfall $< 50\,\text{mm}\,\text{h}^{-1}$) and significant SDHR (hourly rainfall $\geq 50\,\text{mm}\,\text{h}^{-1}$) reports. Hail reports were divided into small hail ($5 \leq$ hail diameter $< 10\,\text{mm}$) and large hail (hail diameter $\geq 10\,\text{mm}$) reports. THW reports were divided into ordinary THW ($17.2 \leq$ wind speed $< 24\,\text{m}\,\text{s}^{-1}$) and significant THW (wind speed $\geq 24\,\text{m}\,\text{s}^{-1}$) reports. The thresholds used herein were the same as those in Z13.

b. *Definitions of SCSs, convection initiation, and decay*

The following criteria must be met to be identified as a SCS:

1) The storm had to persist for at least 1 h in radar images;
2) The storm had to attain a peak radar echo of at least 35 dBZ;
3) The area of echoes above 10 dBZ had to be greater than $6\,\text{km} \times 6\,\text{km}$;
4) The storm had to cause SCW reports (including SDHR, THWs, and hail) at a minimum of five stations during its lifetime.

The first three criteria were basically the same as those in G08 and LC11. The last criterion was used to assure the severity of convective storms. Using the above criteria, SCSs were selected for our study period by examining radar images and the occurrences of three types of SCW. As we intended to document the initiation and decay of SCSs, those that initiated elsewhere and moved into North China and those that initiated beyond the radar detection range were not considered. This led to an exclusion of 336 SCSs during the 7-yr period. When a SCS moved out of North China, tracking was continued using observations from radar stations outside of North China to confirm its decay, and the SCW reports outside of North China region were included in the dataset. If a SCS decayed outside of radar detection range, it was eliminated. A total of 60 SCSs were eliminated on this account. Besides, a total of 367 SCSs were discarded due to missing radar data. Nevertheless, an examination of the spatial distribution and diurnal variation of the initiation of SCSs with identifiable initiation information among all eliminated SCSs showed that the statistics were not influenced by the exclusion of these SCSs (figures not shown), indicating robustness of the results in the present study.

The location and time of convection initiation and decay were determined for each identified SCSs. It is common practice in relevant studies to define convection initiation using a radar reflectivity threshold and an echo area threshold (e.g., Wilson and Roberts 2006; Weckwerth et al. 2011; Mulholland et al. 2018). For the purposes of this study, the convection initiation and decay were defined as the first and last appearances of radar echoes ≥ 35 dBZ reaching an area of at least 6 km $\times$ 6 km, respectively. The initiation and decay locations were determined objectively using an algorithm similar to that of Li et al. (2012) and Yang et al. (2019). This algorithm performed storm identification based on the theory of pattern recognition and matching in the field of digital image processing technology. Specifically, the border of the 35-dBZ echoes of the SCS at convection initiation/decay time was first obtained through an eight-neighborhood technique (Thurfjell et al. 1995), and the centroid of the enclosed area was subsequently determined as the convection initiation/decay location. In addition, if there were no convective echoes (radar reflectivity ≥ 40 dBZ, Geerts 1998; Parker and Johnson 2000) observed within 100 km and in the preceding 30 min of a newly initiated convection, we considered this convection a pristine one (Bai et al. 2020). Otherwise, the convection was considered as secondary convection initiated by a previous convective storm and was not included in our dataset. Storm tracking was performed subjectively in this study.

c. *Classification of storm morphologies*

The classification scheme used in the present study was basically the same as that in G08, except with an addition of the EL type. EL systems were added because we found they were relatively common in the study area. Specifically, the storm morphologies were classified into three major types, namely, cellular, linear, and nonlinear. The cellular storms were subdivided into individual cells (ICs), clusters of cells (CCs), and broken lines (BLs). ICs were storms without weaker radar echoes ($10 <$ radar echoes < 40 dBZ, i.e., above the radar noise level and below the reflectivity threshold for convective echoes) connecting the cells. CCs were storm cells connected by weaker radar echoes. BLs were individual cells arranged in a linear fashion without the convective echoes being connected. Linear systems were those in which the convective echoes were connected and organized in a linear fashion of at least 75 km in length and a length-to-width ratio of at least 3:1, with these features lasting for at least 30 min. The criteria for linear systems generally agree with those in previous studies (Klimowski et al. 2003; G08; Schoen and Ashley 2011; Z13; Yang et al. 2019). The linear systems included six subtypes: convective lines with no stratiform (NSs), TSs, LSs, PSs, ELs, and BEs. BEs were those with convective echoes appearing as crescent- or bow-shaped. This shape was quantitatively defined by the ratio of its arc length to the straight-line distance between the two endpoints of the convective echoes being at least 1.2:1 (Z13). In addition, the bowing echo was required to exhibit an increasing radius with time or a persistent arc to differentiate it from a coincident arc-like structure (Klimowski et al. 2003; Schoen and Ashley 2011). BEs were not required to have a stratiform precipitation region. If a linear system was not classified as a BE, it was then deemed as one of the five remaining subtypes. The discrimination among these five linear subtypes was based on the presence and arrangement of stratiform and convective precipitation using the criteria same as those in Parker and Johnson (2000) and Z13. Finally, NLs were those with convective echoes organized in a connected but nonlinear fashion. Examples illustrating the classified 10 morphologies from real cases are given in Fig. 3. Additionally, if a morphology was not able to be identified owing to poor-quality radar data, it was marked as null.

The morphology classification was performed after the selection of SCSs and determination of convection initiation and decay. For each identified SCS, radar images during its lifetime were examined chronologically to identify and classify storm morphologies that were associated with SCW reports (i.e., we focused only on storm morphologies that caused SCW reports rather than all morphologies appearing during the lifetime of the SCS). To do this, we started with the first SCW report and associated it with the appropriate radar morphology, and repeated this for every other report during the lifetime of the SCS. Some studies classified the storms based on the dominant storm morphology (e.g., Parker and Johnson 2000), while others assigned the SCW to the storm type that immediately caused it (e.g., Klimowski et al. 2003; Schoen and Ashley 2011; Smith et al. 2012; Z13). The latter was used in the present study. We are aware, however, that such an assignment has the risk of designating a SCW to a transient morphology that is not truly responsible. Therefore, it was required that a morphology persist for at least 30 min to be included in the dataset, as has done in Lombardo and Colle (2010). A minimum duration of 30 min should be long enough to prevent assigning a SCW report to a transient morphology, while being small enough to prevent assigning the SCW report to a wrong morphology. If the 30-min criterion was not met, the SCW was assigned to the last qualified morphology.

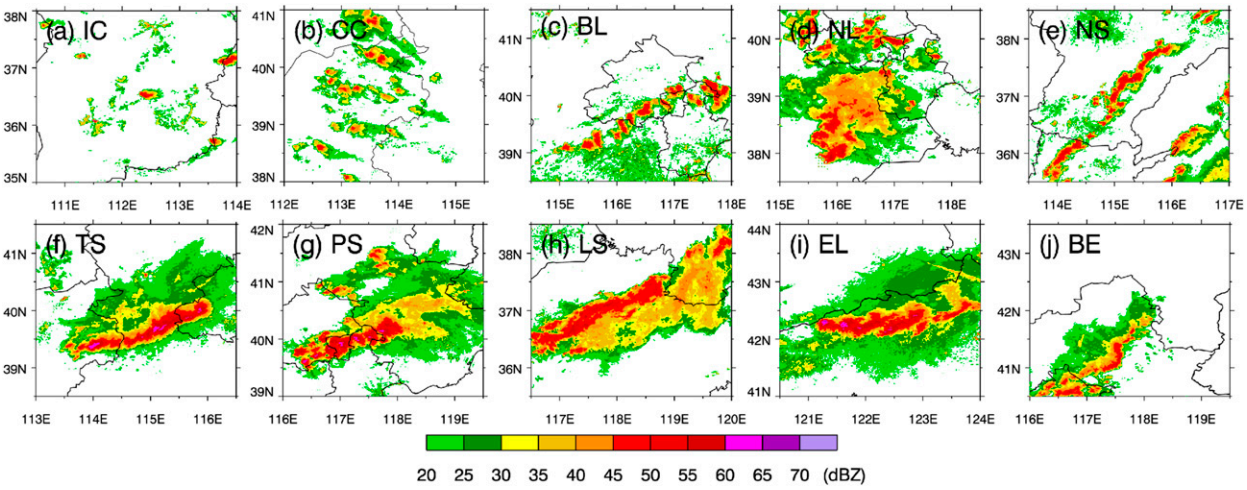

FIG. 3. Composite radar reflectivity images illustrating the 10 storm morphologies classified in the present study: (a) IC at 1250 BST 10 Jun 2016, (b) CC at 1406 BST 12 Jun 2017, (c) BL at 2250 BST 15 Aug 2013, (d) NL at 2030 BST 21 Jul 2015, (e) NS at 1718 BST 13 Aug 2018, (f) TS at 2006 BST 13 Jul 2017, (g) PS at 2248 BST 11 Aug 2017, (h) LS at 0400 BST 28 Jul 2013, (i) EL at 2042 BST 13 Jul 2017, and (j) BE at 2210 BST 12 Sep 2013.

3. Results

a. Initiation, decay, and lifetime of the SCSs

A total of 371 SCSs were identified during the 7-yr period over North China, with the most occurring in July (116 cases) and the second most in August (111 cases). This was consistent with the longstanding perception that the convection and precipitation over North China occur primarily in these two months (Tao 1980). Figure 4 shows the geographical distribution of the occurrence frequency of convection initiation and decay. Convection initiation was observed in most of the study area with favored locations. For example, the maximum frequency was located over the high terrain of Mount Taihang (37°–38°N, 113°–114°E, the names of mountains and cities/provinces are given in Fig. 1) with 17 convection initiation events in one grid box. The second and third highest frequencies appeared near Mount Tai (36°–37°N, 117°–118°E) and Mount Taiyue (36°–37°N, 112°–113°E) with 14 and 12 convection initiation events per grid box, respectively. Other geographical hotspots included Mount Yunzhong (38°–39°N, 112°–113°E), the foothill of Mount Taihang nearing the middle-west border of Hebei province (38°–39°N, 112°–113°E), southern Beijing (39°–40°N, 116°–117°E), and the boundaries between Hebei and Shandong provinces (37°–38°N, 116°–117°E). The finding that convection initiation was favored in mountainous areas was also documented in previous studies (e.g., Aoshima et al. 2008; Weckwerth et al. 2011). SCSs tended to decay at the following preferred locations: northeastern Hebei (around 40°N, 119°E), the mideast of Shandong province (around 37°N, 119°E), and northern Henan (around 36°N, 114°E).

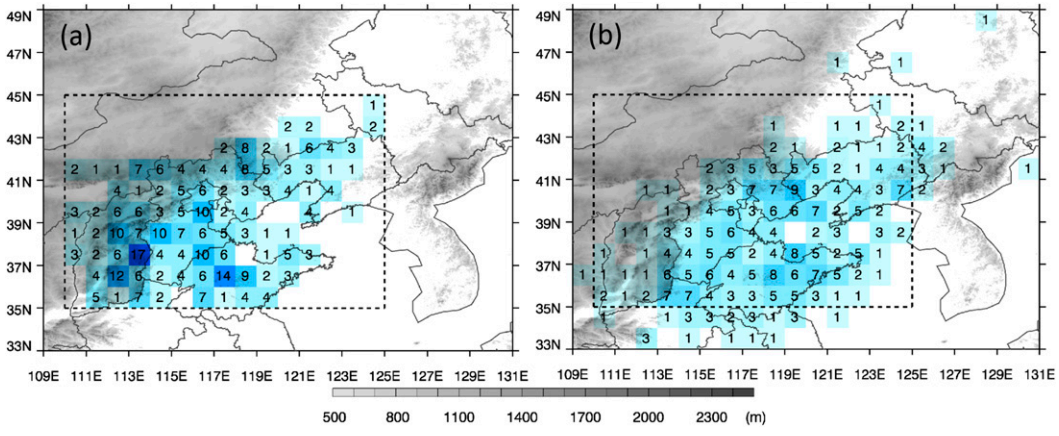

FIG. 4. Geographical distribution of the occurrence frequency of (a) initiation and (b) decay of the identified 371 SCSs in 1° × 1° grid squares. The frequency is shown by the number in each grid with higher frequency indicated by darker blue shading. Gray shading represents topography. The dashed rectangle marks the region used for convection initiation identification (i.e., North China).

Convection initiation showed a stronger tendency to cluster in space than convection decay (the maximum frequency in a grid box was 17 for initiation and 9 for decay).

The diurnal variation of convection initiation and decay is given in Fig. 5a. The majority (58.5%) of convection initiation occurred during 1000–1500 BST with a peak at 1200–1300 BST and a close secondary peak at 1100–1200 BST. This indicated that convection over this region was primarily a result of the diurnal variation of solar heating. However, closer inspection of Fig. 6a suggested that, while most SCSs initiated around noon over the study area, a number of SCSs over the plains of Hebei Province and Beijing initiated during the early evening to early morning (i.e., 1800–0600 BST of the next day). This was consistent with the results of previous studies (He and Zhang 2010; Chen et al. 2012; Bao and Zhang 2013), which suggested that storms occurred primarily at night over the North China plains due to favorable nocturnal initiation and intensification mechanisms such as mountain-plains solenoid circulation and nocturnal low-level jet. Most SCSs decayed at night (Figs. 5a and 6b) with a peak at 2100–2200 BST. More than half (58.5%) of the SCSs had a lifetime of 7–13 h, with the peak being 7–8 h (Fig. 5b). The average lifetime of the SCSs was 11.4 h, which was shorter than that of the MCSs over central East China (14 h, Z13). This could be partly due to the different criteria for convection initiation and decay in two studies. The minimum and maximum lifetime of the SCSs were 3.3 h and 31.2 h, respectively.

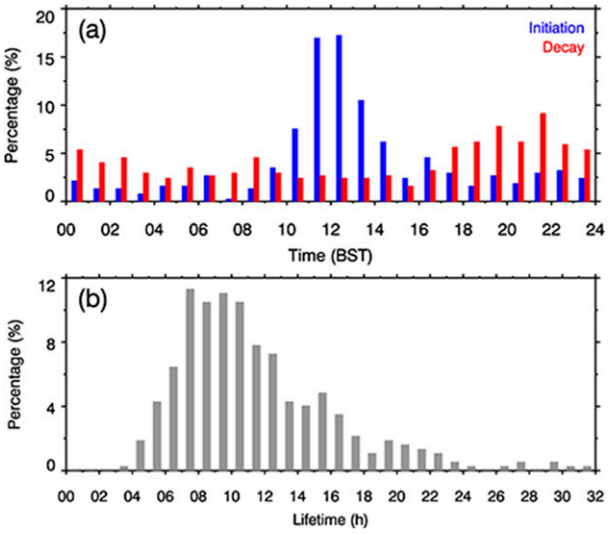

FIG. 5. Histograms of the (a) convection initiation (blue) and decay (red) time and (b) lifetime of the identified 371 SCSs.

b. Storm morphologies and associated SCW

A total of 1429 SCW-producing morphologies were identified from the 371 SCSs. The percentage distribution of the 11 morphologies is given in Fig. 7a. Of the three major morphologies (i.e., cellular, nonlinear and linear), nonlinear was most common, making up more than one-third (37.8%) of all morphologies. Cellular was the next most common type, composing slightly less than one-third (30.6%) of all morphology samples. Linear systems made up 26.3% of the morphologies. The remaining 5.3% were null type. CCs dominated the cellular type with a proportion of 80.8%. Among linear systems, TSs were most prevalent with a proportion of 27.4%, followed closely by NSs (26.6%), while the remaining were composed of PSs (17.8%), ELs (14.6%), BEs (9.0%), and LSs (4.5%). One commonality of the morphology percentage distribution between North China and central east China (Z13) was that there was no dominant linear morphology over both regions. However, EL systems made up a much smaller proportion in linear systems over North China (14.6%) than over central east China (22.7%). The morphology distribution differed from that of G08 and Lombardo and Colle (2010) in that the proportion of cellular storms was lower in the present study. The discrepancy could be partly attributed to the different study objects in these studies. G08 and Lombardo and Colle (2010) examined the morphologies of all convective storms, whereas the present study focused on the SCW-producing morphologies of SCSs. Though the restrictions for convective storms (i.e., criteria 1–3 in the definition of SCSs in section 2b) were largely the same for these studies, a requirement of at least five stations recording SCW reports was used in the present study. Therefore, convective storms with lower productivity of SCW (e.g., isolated cells or loosely organized cellular storms) were filtered out in our selection of SCSs. Also, only SCW-producing morphologies (rather than all morphologies) were identified and classified in this study, while all convective elements were included in G08 and Lombardo and Colle (2010). Since cellular morphologies were generally less likely to be associated with SCW (G08), they made up a less proportion in our morphology sample.

A total of 15 966 SCW reports (including 15 355 SDHR, 172 hail, and 439 THWs) were identified as being associated with the 1429 morphology samples. Figure 7b shows the percentage distribution of SCW reports (the sum of SDHR, hail, and THWs) among the 11 morphologies. Of the three major morphologies, linear systems produced the most SCW reports (44.4%), though they occurred least frequently (26.3%). Conversely, cellular storms composed 30.6% of the morphology sample, but they only contributed to 10.7% of the SCW reports. Nonlinear systems contributed to 41.5% of the SCW reports. Of the 10 specific morphologies (i.e., all morphologies except for null), NL systems were associated with the greatest number of reports, followed by TS, PS, CC, NS, and BE systems. No other morphology made a contribution of greater than 5%. Note that NS systems had a very close occurrence frequency to TS systems (Fig. 7a), but they produced only approximately half of the SCW reports as TS systems. This indicated the TS systems were almost twice as efficient as NS systems in producing SCW. The above percentage distribution appeared to vary greatly from those of LC11 (their Fig. 2) and G08 (their Fig. 8a). This could be attributed to the different SCW reports under investigation. The SCW reports in G08 and LC11 included hail, wind, and tornadoes. It is documented in LC11 that wind, hail, and tornado reports made up 67.6%, 31.8%, and 0.6%, respectively, of the dataset. By contrast, the SCW reports in this study comprised an overwhelming portion (96.2%) of SDHR reports and a small portion (3.8%) of hail and THW

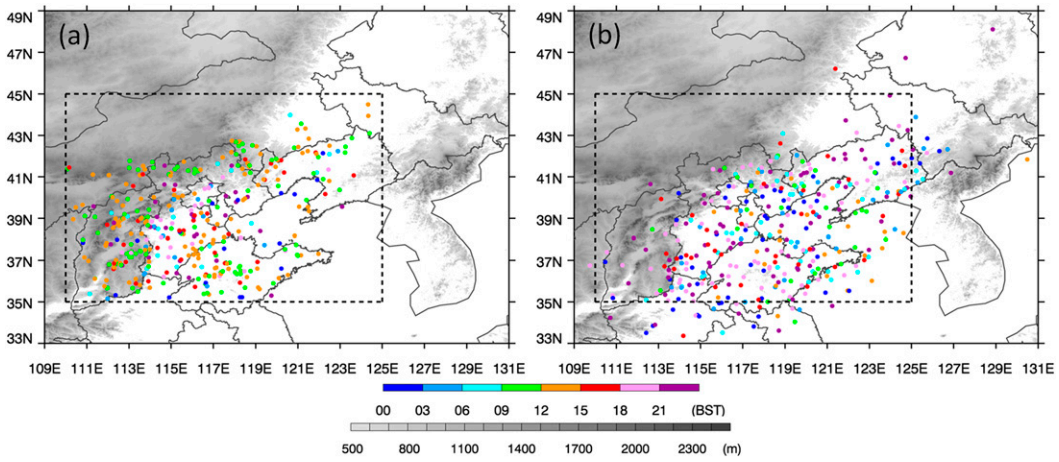

FIG. 6. Geographical distribution of location and time of (a) initiation and (b) decay of the identified 371 SCSs. The color of the dots represents convection initiation/decay time. Gray shading represents topography. The dashed rectangle marks the region used for convection initiation identification (i.e., North China).

reports. Since cellular storms were abundant producers of hail and THWs (LC11), these systems made up a larger proportion in G08 and LC11. In addition, the distribution of flooding events among different morphologies was also examined in G08 (their Fig. 8b). Though the occurrence of flooding was associated with not only the rainfall intensity but also the duration of the rainfall, among other factors (Doswell et al. 1996), similarities were observed between their Fig. 8b and Fig. 11 in this study. For example, NL systems were the leading producers of flooding/SDHR, followed by TS systems.

The monthly variation of the number of 11 morphologies is shown in Fig. 8. The total number of all morphologies reached its peak in July, followed by August, June, September, and May, which was in accordance with the monthly variation of SCSs number. Both cellular and linear storms showed a peak in July, whereas nonlinear systems reached a peak in August. For each of the 10 morphologies, ICs, CCs, ELs, and BEs peaked in July, while BLs, NLs, TSs, PSs, and LSs peaked in August. NSs were equally frequent in July and August. This was different from the results over central east China (Z13), which indicated that nonlinear systems and five types of linear systems (NSs, TSs, LSs, PSs, and ELs) peaked in July whereas BE systems peaked in June. Compared with the results over the United States (G08; Lombardo and Colle 2010), the peak months of these morphologies showed greater uniformity over China.

Figure 9 shows the distribution of three types of SCW reports as functions of storm morphology and month. SDHR occurred primarily in July and August with a peak in July, hail occurred primarily in June, and THWs occurred primarily in June and July with a peak in June. This corresponded

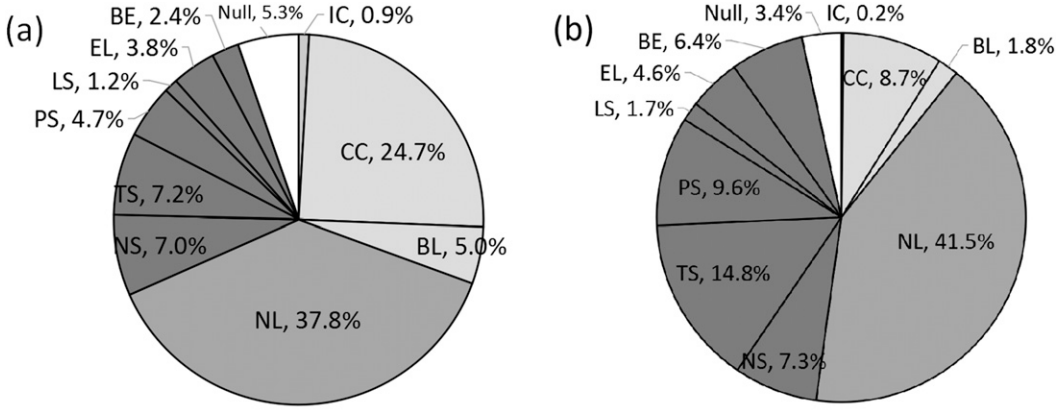

FIG. 7. Percentage distribution of the (a) occurrence frequency of 11 morphologies, and (b) 15 966 SCW reports among the 11 morphologies. Light shading represents cellular storms (i.e., ICs, CCs, and BLs), darker shading represents nonlinear systems (i.e., NLs), the darkest shading represents linear systems (i.e., NSs, TSs, PSs, LSs, ELs, and BEs), and no shading represents the null type.

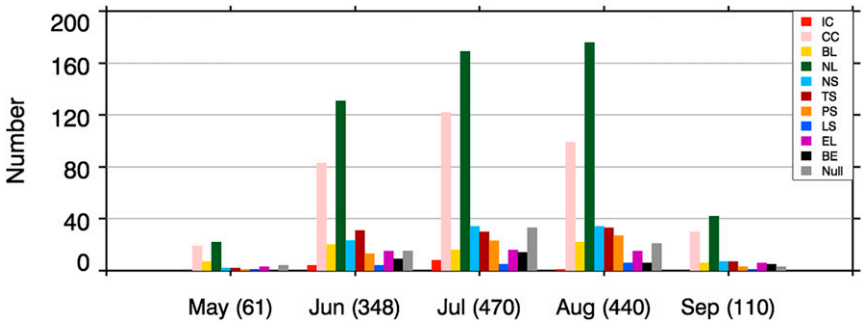

FIG. 8. Monthly variation of the number of 11 storm morphologies. The total number of all morphologies in each month is shown in parentheses in the abscissa axis.

well with the prevalent recognition of SCW occurrences over North China (J. Chen et al. 2013a; Yang et al. 2017; Li et al. 2018). For SDHR, IC, CC, NL, TS, LS, and EL systems produced the greatest number of reports in July, whereas BL and BE systems produced the most reports in June. NSs and PSs were associated with the most SDHR reports in August. Hail, among the three types of SCW, showed the greatest consistency among different morphologies regarding the peak month of reports: despite that BLs and ELs produced the most hail reports in May and August, respectively, the majority of the morphologies were associated with the greatest number of hail reports in June. As a matter of fact, most of the morphologies that had a June peak were associated with about twice as many hail reports in June as in the next most active month, which indicated that June dominated the hail production over the five warm season months. In addition, none of the 10 morphologies had a peak occurrence frequency in June (Fig. 8), which further implied that morphologies except for BLs and ELs were much more efficient in producing hail in June compared with other months. For THWs, CCs, BLs, and TSs caused the greatest number of reports in June, NLs produced the most reports in July, while ELs and BEs showed the most reports in August. The total number of THW reports by five linear subtypes (NSs, TSs, PSs, LSs, and ELs) showed a peak in June. This was in agreement with the results of Yang and Sun (2018), which indicated that THWs-producing linear convective systems showed a preferential development in June.

The distribution of each type of SCW reports as a function of storm morphology is also examined (Fig. 10). Linear systems produced the most SDHR reports (6877, 44.8% of all SDHR reports), followed closely by nonlinear systems (6368, 41.5% of all SDHR reports). Cellular storms produced significantly fewer SDHR reports (1573, 10.2% of all SDHR reports) in comparison. Among the 10 specific morphologies, NL systems dominated the SDHR production, followed by TS and PS systems. CCs were also relatively abundant producers of SDHR reports, mainly owing to their frequent occurrence (Fig. 7a). Two types of cellular storms (ICs and BLs) made the least contribution to SDHR reports among 10 morphologies. Cellular and nonlinear storms produced comparable hail reports (65 and 69, respectively), which was slightly more than twice of the reports produced by linear systems (31). Of the 10 morphologies, NLs and CCs produced distinctly more hail reports than the remaining morphologies. Another cellular type, BLs, were also relatively effective in producing hail. Nonlinear systems produced the most THW reports (185, 42.1% of all THW reports), followed closely by linear systems (176, 40.1% of all THW reports). Cellular storms were responsible for 16.6% of the THW reports. Among linear morphologies, TSs, BEs, and ELs produced significantly more THW reports than the remaining morphologies (i.e., NSs, PSs, and LSs). PS and LS systems also produced the fewest THW events in LC11. LSs, among all linear systems, were associated with the fewest number of SDHR, hail, and THW reports. This was also observed in LC11. A notable difference between the results of the present study and those of LC11 was that NS systems

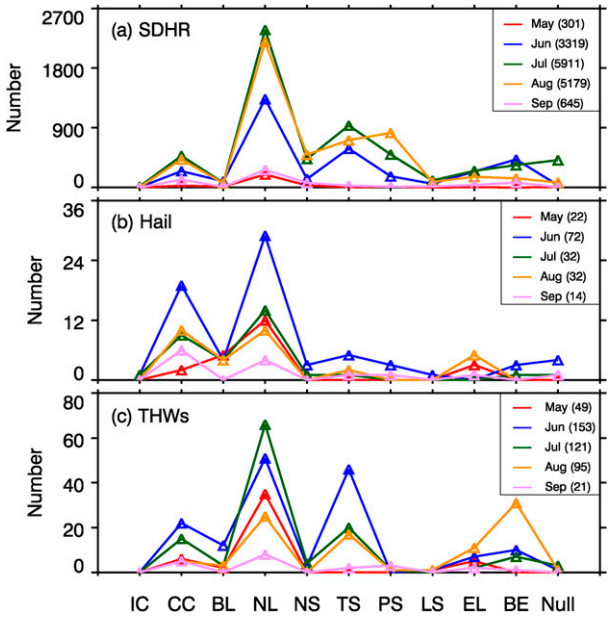

FIG. 9. Distribution of (a) SDHR, (b) hail, and (c) THW reports as functions of storm morphology and month. The monthly sums of reports over the 7-yr period are shown in the parentheses in the legend.

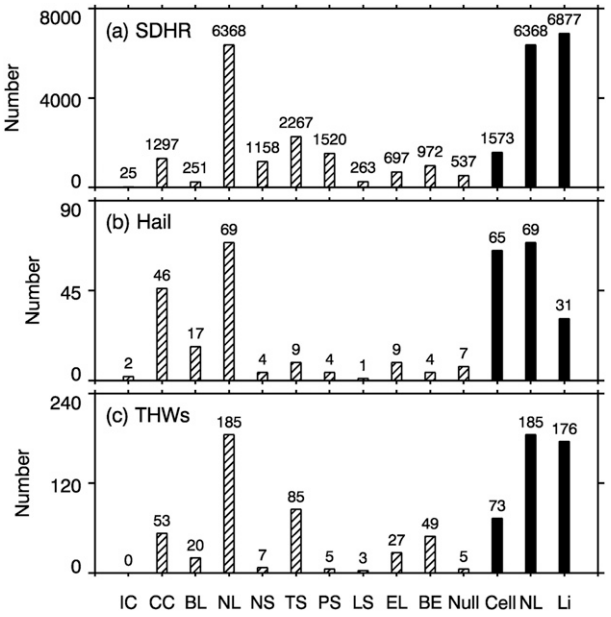

FIG. 10. Number of (a) SDHR, (b) hail, and (c) THW reports associated with 11 specific morphologies (bars filled with parallel lines) and 3 major morphologies (solid black bars). The SCW reports referred to those identified as being associated with the 1429 morphology samples. Numbers of reports are given above each bar.

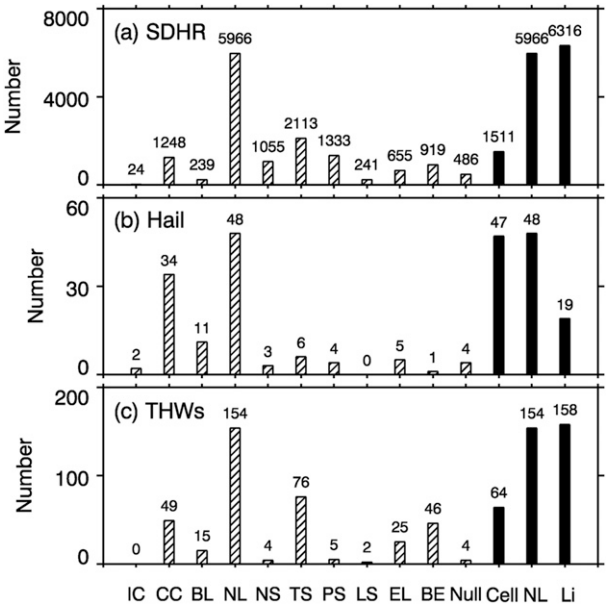

FIG. 11. As in Fig. 10, but for (a) ordinary SDHR ($20 \leq$ hourly rainfall $< 50\,\text{mm}\,\text{h}^{-1}$), (b) small hail ($5 \leq$ diameter $< 10\,\text{mm}$), and (c) ordinary THWs ($17.2 \leq$ wind speeds $< 24\,\text{m}\,\text{s}^{-1}$).

produced far fewer hail and THW reports over North China than over the northeast United States. This inconsistency may be explored in future studies.

The three types of SCW were further stratified based on severity to investigate their relations with storm morphologies (Figs. 11 and 12). The distribution of three types of SCW with weaker intensity (i.e., ordinary SDHR, small hail, and ordinary THWs) was largely the same with that of all SCW reports. However, differences arose when considering SCW with stronger intensity (i.e., significant SDHR, large hail, and significant THWs). The significant SDHR reports produced by PSs outnumbered those by TSs, making PSs the most prolific linear systems of significant SDHR. Among the linear systems, ELs produced the greatest number of large hail. Despite that BLs produced less than one-third of the ordinary THW reports compared with CCs, they were associated with more significant THW reports than CCs.

Since the total number of SCW reports associated with a morphology was influenced by the occurrence frequency of that morphology, the former was divided by the latter to arrive at the number of reports per morphology. The results are shown in Fig. 13. For SDHR, linear systems were the most efficient producers with an average number of 18.29 reports per morphology. Nonlinear and cellular storms came in second and third places, respectively. Among the 10 specific morphologies, BEs produced evidently more SDHR reports per morphology than other systems. PS systems had the second greatest number of SDHR reports per morphology, followed closely by TS systems. NL systems had lower efficiency than all linear morphologies except NSs. The three types of cellular storms had remarkably lower efficiencies at producing SDHR compared with other morphologies. For hail, cellular storms had the highest efficiency, which corresponded well with the results over the United States (G08; LC11). Among the 10 specific morphologies, BLs produced the greatest number of hail reports per morphology. Over the central United States, it was

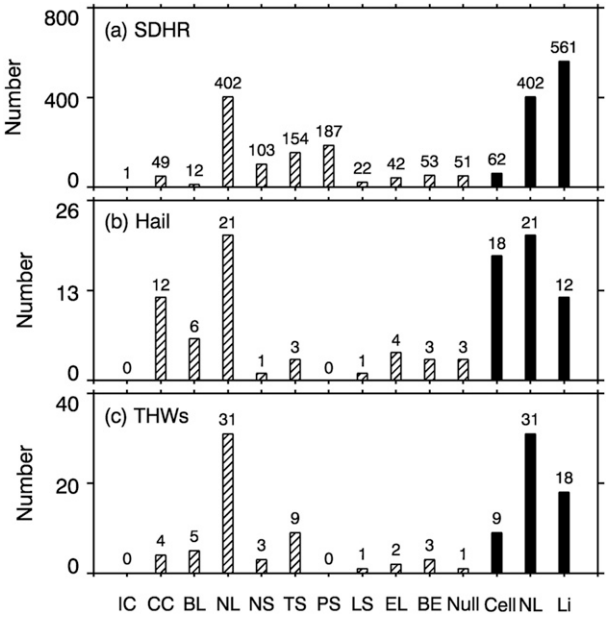

FIG. 12. As in Fig. 10, but for (a) significant SDHR (hourly rainfall $\geq 50\,\text{mm}\,\text{h}^{-1}$), (b) large hail (diameter $\geq 10\,\text{mm}$), and (c) significant THWs (wind speeds $\geq 24\,\text{m}\,\text{s}^{-1}$).

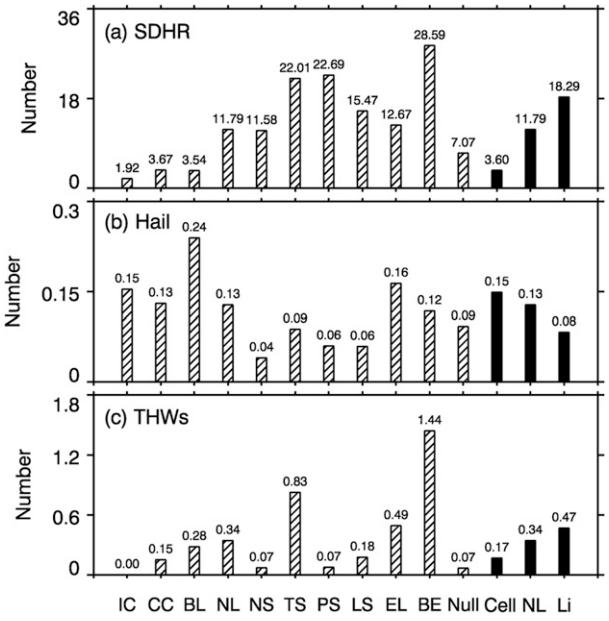

FIG. 13. Number of (a) SDHR, (b) hail, and (c) THW reports normalized by the occurrence frequency of each specific morphology (bars filled with parallel lines) and each major morphology (solid black bars). Normalized numbers are given above each bar.

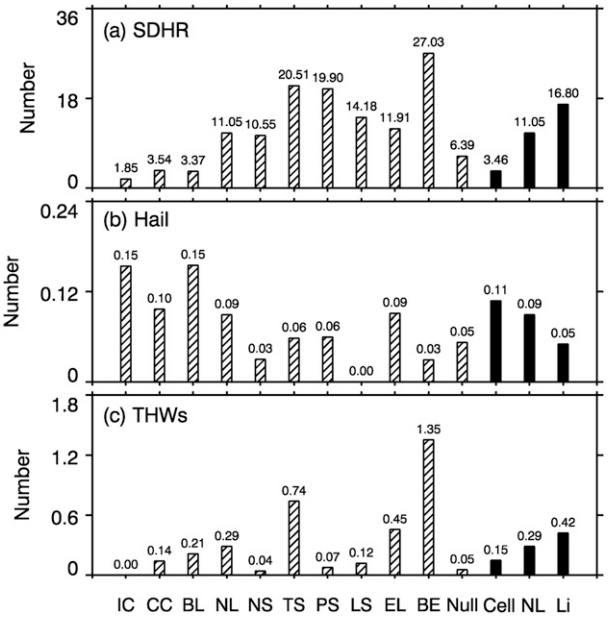

FIG. 14. As in Fig. 13, but for (a) ordinary SDHR ($20 \leq$ hourly rainfall $< 50\,\text{mm}\,\text{h}^{-1}$), (b) small hail ($5 \leq$ diameter $< 10\,\text{mm}$), and (c) ordinary THWs ($17.2 \leq$ wind speeds $< 24\,\text{m}\,\text{s}^{-1}$).

also found that hail of all sizes was fairly frequent for BL systems (G08). Among the six linear morphologies, ELs had the highest efficiency for hail production, followed by BEs and TSs. The high average number of ICs was likely a result of the small sample size of this morphology, and the number is likely to reduce if a larger sample size is available. A similar problem has been documented in Snook and Gallus (2004).

For THWs, linear systems produced the greatest number of reports per morphology, followed by nonlinear and cellular storms. Of the 10 morphologies, BEs were associated with a remarkably higher number of THW reports per morphology than any other morphology. TS systems were associated with the second highest number of THW reports per morphology. This is not surprising since TS systems often have rear-inflow that can cause damaging winds upon reaching the surface (Smull and Houze 1987). BEs and TSs were also the top two active morphologies for THWs over the central United States (G08). Over the Northeast United States, it was found that TS (BE) systems were associated with the most (second most) wind reports per event (LC11). Among the three cellular types, BLs were associated with nearly twice as many THW reports per morphology as CCs. The finding that BL systems produced nearly twice as many of both hail and THW reports per morphology as CCs indicated that cells organized in a linear fashion were more prone to generate hail and THWs than disorganized cells. NSs were the least efficient linear morphology for SDHR, hail, and THW reports, which was in line with the result over the central United States (G08) but different from that over the Northeast United States (LC11).

The average number of SCW reports with different severities by per morphology was also examined (Figs. 14 and 15). The distribution of ordinary THW reports was basically the same as that of all THW reports. This was also true for SDHR, except that TSs had a slightly higher number of ordinary SDHR reports per morphology than PSs. The distribution of small hail reports showed differences from that of all hail reports. For significant SDHR, the three types of cellular storms produced much fewer reports per morphology compared with nonlinear and linear systems. All linear systems had higher numbers of reports per morphology than nonlinear systems. PS systems, though produced approximately only 74% of ordinary SDHR reports per morphology as BE systems (Fig. 14a), were responsible for approximately 1.8 times as many significant SDHR reports per morphology as BE systems. It was also concluded in Z13 that, PS systems were apt to produce intense rainfall, especially extreme rainfall events, owing to the abundant moisture in the environment associated with these systems. Over the United States, PS systems were found to be substantial flash flood producers since they entailed both the along-line movement of hydrometeors and back-building of convective cells (G08; Schumacher and Johnson 2005; Parker 2007a,b). BE and TS systems were the second and third most efficient morphologies for significant SDHR, respectively.

BEs had the greatest number of large hail reports per morphology. Over the central United States, it was found that BE systems had the highest frequency per case for hail reports of less than 1-in. diameter (G08) (1 in. = 2.54 cm). According to a recent study of a 36-yr hail climatology over China (Li et al. 2018), only 5.5% (10.5%) of the hail records had diameters $\geq 20\,\text{mm}$ in the mountains (plains) of North China. It was thus deduced that the majority of large hail reports (i.e., diameter $\geq 10\,\text{mm}$) in the present study fell into the 1-in. diameter category of G08. Therefore, the results in the present

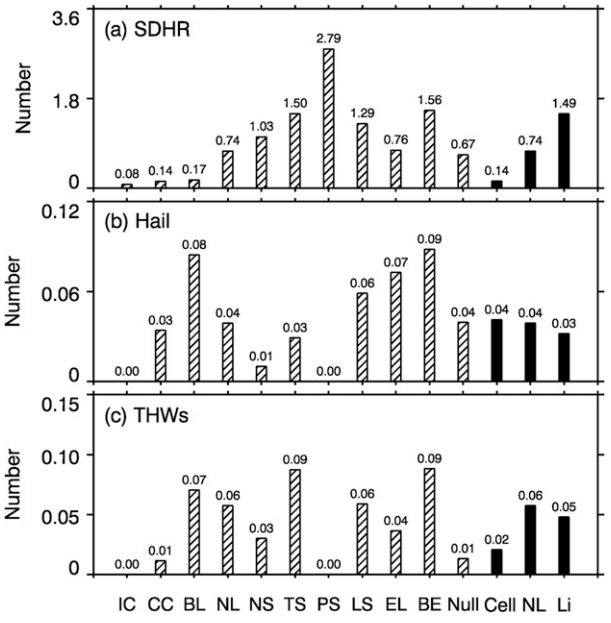

FIG. 15. As in Fig. 13, but for (a) significant SDHR (hourly rainfall $\geq 50\,\text{mm}\,\text{h}^{-1}$), (b) large hail (diameter $\geq 10\,\text{mm}$), and (c) significant THWs (wind speeds $\geq 24\,\text{m}\,\text{s}^{-1}$).

study agree well with that of G08. BLs were the next most efficient producers of large hail. No large hail reports were associated with PS systems. Z13 also observed that none of the hail reports were associated with PS systems over central east China. However, over the central United States, it was found that PS systems had the greatest number of reports per case for hail with ≥ 2-in. diameter (G08). The sharp differences in hail threat by PS systems between China and the United States may be attributable to the environmental condition (e.g., moisture and vertical wind shear) differences in two regions. For example, Z13 found that, the environment of PS systems featured abundant moisture with precipitable water of 62.8 mm, which was the second largest among the six linear types of systems classified in their study, while over the central United States PS systems arose in environment with a minimum precipitable water among TS, PS, and LS systems (Parker and Johnson 2000). In addition, studies (e.g., Parker and Johnson 2000; Parker 2007a,b) have shown that, PS systems occurred in environments with significant deep-layer wind shear and clockwise-turning hodographs, similar to those of supercells. This helps to understand why PS systems have the greatest number of larger hail reports per morphology over the United States. These results suggest that the mechanisms for the development of PS systems over China and the United States are different, and further studies are needed to explore the differences. For significant THWs, nonlinear systems showed higher number of reports per morphology than linear systems. Of the 10 classified morphologies, the greatest numbers of reports per morphology were present for BE and TS systems. BL systems were also relatively efficient producers of significant THWs.

We further explored the correspondence between storm morphologies and the following seven types of severe weather: only SDHR; only hail; only THWs; SDHR and hail; SDHR and THWs; hail and THWs; and SDHR, hail, and THWs (Fig. 16). The percentage distribution of IC and LS systems were not discussed because of their limited sample sizes. It was readily seen that SDHR-only weather was the most common type for all morphologies. This was especially true for two linear systems (NSs and PSs), for whom the percentages reached over 90% among seven weather types. The lowest percentage of SDHR-only weather was observed for BLs, a consequence of higher percentages of other weather types associated with these systems. Cellular storms, especially BLs, had higher percentages of hail-only as well as THWs-only weather than other systems. PS and BE systems were not associated with hail-only and THWs-only weather in this study, which indicated that hail or THWs by these systems was always accompanied by SDHR. TS systems were not associated with hail-only weather. The highest percentage of SDHR-and-hail weather was observed for BL systems, followed by BE, NL,

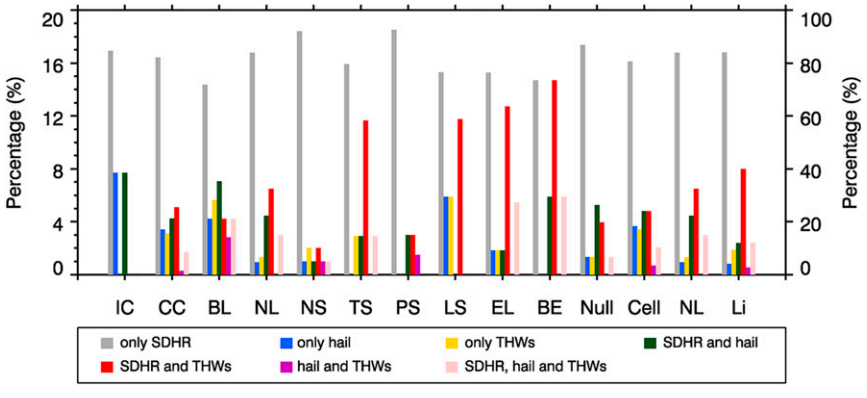

FIG. 16. Percentages of seven severe weather types associated with each morphology. The seven weather types are as follows: only SDHR; only hail; only THWs; SDHR and hail; SDHR and THWs; hail and THWs; and SDHR, hail, and THWs. The values for the first type (i.e., only SDHR) are given in the right *y* axis while those for the remaining six weather types are given in the left *y* axis.

and CC systems. Higher percentages of severe weather featured both SDHR and THWs were evident for three linear systems, namely, BEs, ELs, and TSs. Severe weather with both hail and THWs rarely occurred over North China with only sporadic appearances in CC, BL, NS, and PS systems. The highest percentage of severe convective weather that featured the concurrence of SDHR, hail, and THWs was observed in BE systems, followed closely by EL systems.

4. Conclusions

Using SWRs, precipitation observations, and composite Doppler radar reflectivity data, this work established a 7-yr climatology of the initiation and decay, as well as the morphologies and associated SCW of SCSs during the warm seasons of 2011–18 (except 2014) over North China. Our main findings are as follows.

1) A total of 371 SCSs were identified for the 7-yr period over North China. The initiation of SCSs was found in most of the study area, with preferred locations near mountains and a peak month of July. The majority of the SCSs initiated during 1000–1500 BST owing to daytime radiative heating with a peak at 1200–1300 BST. SCSs mostly decayed over the plains at night. Most SCSs had a lifetime of 7–13 h. The average lifetime was 11.4 h.
2) A total of 15 966 SCW reports (including 15 355 SDHR, 172 hail, and 439 THWs) were identified as being associated with the 1429 morphologies of the 371 SCSs. Linear systems, though occurred least frequently, produced the most SCW reports. Conversely, the cellular storms composed 30.6% of the morphology sample, but only contributed to 10.7% of the SCW reports. Nonlinear systems occurred most frequently and were responsible for 41.4% of the SCW reports.
3) All morphologies except for BLs and ELs were more effective in producing hail in June than in other months. Less consistency was present among different morphologies regarding the peak months of SDHR and THW reports. Of the 10 morphologies, NLs produced the most SDHR reports, the most hail, and the most THW reports, regardless of the severity of the reports. TSs and PSs produced the next most ordinary and significant SDHR reports, respectively. The next most abundant producers of both small and large hail were CCs, and those of both ordinary and significant THW reports were TSs.
4) Linear (cellular) systems were the most efficient producers (i.e., having the greatest number of reports per morphology) of SDHR and THW (hail) reports. For SDHR, BEs and PSs were the most efficient producers of ordinary and significant SDHR, respectively. For hail, BLs and BEs were the most efficient producers of small and large hail, respectively. For THWs, BEs were most efficient in producing both ordinary and significant THWs (TSs were equally efficient in producing significant THWs). The highest percentage of SDHR-only weather was present for PSs, whereas the lowest was observed for BLs as a consequence of the highest proportions of hail- and THWs-related weather.

This work is the first to examine the SCW-producing storm morphologies over North China, focusing mainly on their occurrence frequencies and relations with three types of SCW reports. The results are helpful for local forecasters to better anticipate the storm types and associated hazardous weather. For example, cellular storms are efficient hail producers. Extra caution should be taken when individual cells are organized in a linear fashion (i.e., BL systems), as the hail- and THWs-producing efficiency of these systems is approximately 2 times as high as that when cells are loosely connected as clusters. Of the six linear morphologies, BEs, TSs, and PSs are more hazardous.

Furthermore, similarities and differences are found through comparisons with the results over central east China and the United States. For example, PSs excel at producing significant SDHR over these regions. However, the hail threat by PS systems over China and the United States are significantly different, indicating that more research is needed to explain the geographical differences. Future work could also focus on the geographical distribution of various morphologies, which helps forecasters to anticipate the local morphology types. In addition, analysis is needed concerning the environmental conditions favoring the development of these morphologies and the transition between various morphologies, for example, when and where do the transition occur, and the atmospheric as well as underlying surface conditions that facilitate the transition from one particular type to another.

Acknowledgments. The composite radar reflectivity data, severe weather reports and precipitation observations used in the present study were provided by the National Meteorological Center, China Meteorological Administration. This research was supported by the National Natural Science Foundation of China (Grants 41975056 and 41975057) and Technological Infrastructure project ''Earth System Science Numerical Simulator Facility.''

Data availability statement. A list of the 371 SCS cases identified in this study is provided in a supplemental material.

REFERENCES

Aoshima, F., A. Behrendt, H. S. Bauer, and V. Wulfmeyer, 2008: Statistics of convection initiation by use of Meteosat rapid scan data during the Convective and Orographically-induced Precipitation Study (COPS). *Meteor. Z.*, **17**, 921–930, https://doi.org/10.1127/0941-2948/2008/0337.

Bai, L. Q., G. X. Chen, and L. Huang, 2020: Image processing of radar mosaics for the climatology of convection initiation in South China. *J. Appl. Meteor. Climatol.*, **59**, 65–81, https://doi.org/10.1175/JAMC-D-19-0081.1.

Banta, R. M., 1990: *Atmospheric Processes over Complex Terrain. Meteor. Monogr.*, No. 45, Amer. Meteor. Soc., 323 pp.

——, and C. B. Schaaf, 1987: Thunderstorm genesis zones in the Colorado Rocky Mountains as determined by traceback of geosynchronous satellite images. *Mon. Wea. Rev.*, **115**, 463–476, https://doi.org/10.1175/1520-0493(1987)115<0463:TGZITC>2.0.CO;2.

Bao, X. H., and F. Q. Zhang, 2013: Impacts of the mountain-plains solenoid and cold pool dynamics on the diurnal variation of

precipitation over Northern China. *Atmos. Chem. Phys.*, **13**, 965–6982, https://doi.org/10.5194/acp-13-6965-2013.

Bluestein, H. B., and M. H. Jain, 1985: Formation of mesoscale lines of precipitation: Severe squall lines in Oklahoma during the spring. *J. Atmos. Sci.*, **42**, 1711–1732, https://doi.org/10.1175/1520-0469(1985)042<1711:FOMLOP>2.0.CO;2.

Chen, J., Y. G. Zheng, X. L. Zhang, and P. J. Zheng, 2013a: Distribution and diurnal variation of warm-season short-duration heavy rainfall in relation to the MCSs in China. *Acta Meteor. Sin.*, **27**, 868–888, https://doi.org/10.1007/s13351-013-0605-x.

——, ——, ——, and ——, 2013b: Analysis of the climatological distribution and diurnal variations of the short-duration heavy rain and its relation with diurnal variations of the MCSs over China during the warm season. *Acta Meteor. Sin.*, **71**, 367–382, https://doi.org/10.11676/qxxb2013.035.

Chen, M. X., Y. C. Wang, F. Gao, and X. Xiao, 2012: Diurnal variations in convective storm activity over contiguous North China during the warm season based on radar mosaic climatology. *J. Geophys. Res.*, **117**, 1–14, https://doi.org/10.1029/2012JD018158.

——, ——, X. Xiao, and F. Gao, 2013: Initiation and propagation mechanism for the Beijing extreme rainstorm clusters on 21 July 2012. *Acta Meteor. Sin.*, **71**, 569–592, https://doi.org/10.11676/qxxb2013.053.

Chen, S., Y. C. Wang, W. L. Zhang, and M. X. Chen, 2011: Identifying mechanism of the convective storm moving from the mountain to the plain over Beijing area. *Meteor. Mon.*, **37**, 802–813, https://doi.org/10.7519/j.issn.1000-0526.2011.07.004.

Doswell, C. A., H. E. Brooks, and R. A. Maddox, 1996: Flash flood forecasting: An ingredients-based methodology. *Wea. Forecasting*, **11**, 560–581, https://doi.org/10.1175/1520-0434(1996)011<0560:FFFAIB>2.0.CO;2.

Duda, J. D., and W. A. Gallus, 2010: Spring and summer Midwestern severe weather reports in supercells compared to other morphologies. *Wea. Forecasting*, **25**, 190–206, https://doi.org/10.1175/2009WAF2222338.1.

Fan, L. Q., Y. C. Wang, and M. X. Chen, 2009: Analysis of a severe convective storm event in Beijing using the thermodynamical retrieval method of radar data. *Meteor. Mon.*, **35**, 9–16, https://doi.org/10.7519/j.issn.1000-0526.2009.11.002.

Fan, W. J., and X. D. Yu, 2015: Characteristics of spatial-temporal distribution of tornadoes in China. *Meteor. Mon.*, **41**, 793–805, https://doi.org/10.7519/j.issn.1000-0526.2015.07.001.

Gallus, W. A., N. A. Snook, and E. V. Johnson, 2008: Spring and summer severe weather reports over the Midwest as a function of convective mode: A preliminary study. *Wea. Forecasting*, **23**, 101–113, https://doi.org/10.1175/2007WAF2006120.1.

Geerts, B., 1998: Mesoscale convective systems in the southeast United States during 1994–95: A survey. *Wea. Forecasting*, **13**, 860–869, https://doi.org/10.1175/1520-0434(1998)013<0860:MCSITS>2.0.CO;2.

He, H. Z., and F. Q. Zhang, 2010: Diurnal variations of warm-season precipitation over Northern China. *Mon. Wea. Rev.*, **138**, 1017–1025, https://doi.org/10.1175/2010MWR3356.1.

Hua, S. F., X. Xin, and B. J. Chen, 2020: Influence of multiscale orography on the initiation and maintenance of a precipitating convective system in North china: A case study. *J. Geophys. Res. Atmos.*, **125**, e2019JD031731, https://doi.org/10.1029/2019JD031731.

Karr, T. W., and R. L. Wooten, 1976: Summer radar echo distribution around Limon, Colorado. *Mon. Wea. Rev.*, **104**, 728–734, https://doi.org/10.1175/1520-0493(1976)104<0728:SREDAL>2.0.CO;2.

Klimowski, B. A., M. J. Bunkers, M. R. Hjelmfelt, and J. N. Covert, 2003: Severe convective windstorms over the northern high plains of the United States. *Wea. Forecasting*, **18**, 502–519, https://doi.org/10.1175/1520-0434(2003)18<502:SCWOTN>2.0.CO;2.

Kovacs, M., and D. J. Kirshbaum, 2016: Topographic impacts on the spatial distribution of deep convection over southern Quebec. *J. Appl. Meteor. Climatol.*, **55**, 743–762, https://doi.org/10.1175/JAMC-D-15-0239.1.

Kuo, J. T., and H. D. Orville, 1973: A radar climatology of summertime convective clouds in the Black Hills. *J. Appl. Meteor.*, **12**, 359–368, https://doi.org/10.1175/1520-0450(1973)012<0359:ARCOSC>2.0.CO;2.

Li, J., W. Bin, and W. Dong-Hai, 2012: The characteristics of mesoscale convective systems (MCSs) over East Asia in warm seasons. *Atmos. Ocean. Sci. Lett.*, **5**, 102–107, https://doi.org/10.1080/16742834.2012.11446973.

Li, H. Q., X. P. Cui, and D.-L. Zhang, 2017: On the initiation of an isolated heavy-rain-producing storm near the central urban area of the Beijing metropolitan region. *Mon. Wea. Rev.*, **145**, 181–197, https://doi.org/10.1175/MWR-D-16-0115.1.

Li, X. F., Q. H. Zhang, T. Zou, J. P. Lin, H. Kong, and Z. H. Ren, 2018: Climatology of hail frequency and size in China, 1980–2015. *J. Appl. Meteor. Climatol.*, **57**, 875–887, https://doi.org/10.1175/JAMC-D-17-0208.1.

Liang, Q. Q., S. X. Xiang, L. G. Lin, and W. G. Meng, 2012: MCS characteristics over South China during the annually first rainy season and their organization. *J. Trop. Meteor.*, **28**, 541–551, https://doi.org/10.3969/j.issn.1004-4965.2012.04.013.

Liu, L., Y. C. Wang, and M. X. Chen, 2015: Spatial-temporal evolution characteristics of a squall line in Beijing-Tianjin-Hebei region. *Meteor. Mon.*, **41**, 1433–1456, https://doi.org/10.7519/j.issn.1000-0526.2015.12.001.

Lombardo, K. A., and B. A. Colle, 2010: The spatial and temporal distribution of organized convective structures over the northeast and their ambient conditions. *Mon. Wea. Rev.*, **138**, 4456–4474, https://doi.org/10.1175/2010MWR3463.1.

——, and ——, 2011: Convective storm structures and ambient conditions associated with severe weather over the Northeast United States. *Wea. Forecasting*, **26**, 940–956, https://doi.org/10.1175/WAF-D-11-00002.1.

Meng, Y. N., J. H. Sun, Y. C. Zhang, and S. M. Fu, 2021: A 10-year climatology of mesoscale convective systems and their synoptic circulations in the southwest mountain area of China. *J. Hydrol.*, **22**, 23–41, https://doi.org/10.1175/JHM-D-20-0167.1.

Meng, Z. Y., D. Yan, and Y. J. Zhang, 2013: General features of squall lines in east China. *Mon. Wea. Rev.*, **141**, 1629–1647, https://doi.org/10.1175/MWR-D-12-00208.1.

Mulholland, J. P., S. W. Nesbitt, R. J. Trapp, K. L. Rasmussen, and P. V. Salio, 2018: Convective storm life cycle and environments near the Sierras de Córdoba, Argentina. *Mon. Wea. Rev.*, **146**, 2541–2557, https://doi.org/10.1175/MWR-D-18-0081.1.

Parker, M. D., 2007a: Simulated convective lines with parallel stratiform precipitation. Part I: An archetype for convection in along-line shear. *J. Atmos. Sci.*, **64**, 267–288, https://doi.org/10.1175/JAS3853.1.

——, 2007b: Simulated convective lines with parallel stratiform precipitation. Part II: Governing dynamics and associated sensitivities. *J. Atmos. Sci.*, **64**, 289–313, https://doi.org/10.1175/JAS3854.1.

——, and R. H. Johnson, 2000: Organizational modes of midlatitude mesoscale convective systems. *Mon. Wea. Rev.*, **128**, 3413–3436, https://doi.org/10.1175/1520-0493(2001)129<3413:OMOMMC>2.0.CO;2.

Purdom, J. F. W., 1976: Some uses of high-resolution GOES imagery in the mesoscale forecasting of convection and its behavior. *Mon. Wea. Rev.*, **104**, 1474–1483, https://doi.org/10.1175/1520-0493(1976)104<1474:SUOHRG>2.0.CO;2.

Qin, R., and M. X. Chen, 2017: Impact of a front-dryline merger on convection initiation near a mountain ridge in Beijing. *Mon. Wea. Rev.*, **145**, 2611–2633, https://doi.org/10.1175/MWR-D-16-0369.1.

Schaaf, C. B., J. Wurman, and R. M. Banta, 1988: Thunderstorm-producing terrain features. *Bull. Amer. Meteor. Soc.*, **69**, 272–277, https://doi.org/10.1175/1520-0477(1988)069<0272:TPTF>2.0.CO;2.

Schoen, J. M., and W. S. Ashley, 2011: A climatology of fatal convective wind events by storm type. *Wea. Forecasting*, **26**, 109–121, https://doi.org/10.1175/2010WAF2222428.1.

Schumacher, R. S., and R. H. Johnson, 2005: Organization and environmental properties of extreme-rain-producing mesoscale convective systems. *Mon. Wea. Rev.*, **133**, 961–976, https://doi.org/10.1175/MWR2899.1.

Smith, B. T., R. L. Thompson, J. S. Grams, C. Broyles, and H. E. Brooks, 2012: Convective modes for significant severe thunderstorms in the contiguous United States. Part I: Storm classification and climatology. *Wea. Forecasting*, **27**, 1114–1135, https://doi.org/10.1175/WAF-D-11-00115.1.

Smull, B. F., and R. A. Houze, 1987: Rear inflow in squall lines with trailing stratiform precipitation. *Mon. Wea. Rev.*, **115**, 2869–2889, https://doi.org/10.1175/1520-0493(1987)115<2869:RIISLW>2.0.CO;2.

Snook, N., and W. A. Gallus Jr., 2004: A climatology of severe weather reports as a function of convective system morphology. Preprints, *22nd Conf. on Severe Local Storms*, Hyannis, MA, Amer. Meteor. Soc., P5.5, https://ams.confex.com/ams/11aram22sls/techprogram/paper_81392.htm.

Sun, J. S., and B. Yang, 2008: Meso-β scale torrential rain affected by topography and the urban circulation. *Chin. J. Atmos. Sci.*, **32**, 1352–1364, https://doi.org/10.3878/j.issn.1006-9895.2008.06.10.

——, H. Wang, L. Wang, F. Liang, Y. X. Kang, and X. Y. Jiang, 2006: The role of urban boundary layer in local convective torrential rain happening in Beijing on 10 July 2004. *Chin. J. Atmos. Sci.*, **30**, 221–234, https://doi.org/10.3878/j.issn.1006-9895.2006.02.05.

Tao, S. Y., 1980: *Heavy Rainfalls in China*. Science Press, 225 pp.

Thurfjell, L., E. Bengtsson, and B. Nordin, 1995: A boundary approach for fast neighborhood operations on three-dimensional binary data. *Graph. Models Image Proc.*, **57**, 13–19, https://doi.org/10.1006/gmip.1995.1002.

Wang, X. F., C. G. Cui, W. J. Cui, and Y. Shi, 2014: Modes of mesoscale convective system organization during Meiyu season over the Yangtze River basin. *J. Meteor. Res.*, **28**, 111–126, https://doi.org/10.1007/s13351-014-0108-4.

Weckwerth, T. M., J. W. Wilson, M. Hagen, T. J. Emerson, J. O. Pinto, D. L. Rife, and L. Grebe, 2011: Radar climatology of the COPS region. *Quart. J. Roy. Meteor. Soc.*, **137**, 31–41, https://doi.org/10.1002/qj.747.

Weiss, C. C., and H. B. Bluestein, 2002: Airborne pseudo-dual-Doppler analysis of a dryline-outflow boundary intersection. *Mon. Wea. Rev.*, **130**, 1207–1226, https://doi.org/10.1175/1520-0493(2002)130<1207:APDDAO>2.0.CO;2.

Wilson, J. W., and R. D. Roberts, 2006: Summary of convective storm initiation and evolution during IHOP: Observational and modeling perspective. *Mon. Wea. Rev.*, **134**, 23–47, https://doi.org/10.1175/MWR3069.1.

Xia, R. D., and D.-L. Zhang, 2019: An observational analysis of three extreme rainfall episodes of 19–20 July 2016 along the Taihang Mountains in North China. *Mon. Wea. Rev.*, **147**, 4199–4220, https://doi.org/10.1175/MWR-D-18-0402.1.

Xiao, X., M. X. Chen, F. Gao, and Y. C. Wang, 2013: A mechanism analysis of the thermo-dynamical field of a suddenly intensifying storm from mountains in the Beijing area with the radar data 4DVar. *Acta Meteor. Sin.*, **71**, 797–816, https://doi.org/10.11676/qxxb2013.077.

——, ——, ——, and ——, 2015: A thermodynamic mechanism analysis on enhancement or dissipation of convective systems from the mountains under weak synoptic forcing. *Chin. J. Atmos. Sci.*, **39**, 100–124, https://doi.org/10.3878/j.issn.1006-9895.1403.13318.

Yang, R. Y., Y. C. Zhang, J. H. Sun, S. M. Fu, and J. Li, 2019: The characteristics and classification of eastward-propagating mesoscale convective systems generated over the second-step terrain in the Yangtze River Valley. *Atmos. Sci. Lett.*, **20**, e874, https://doi.org/10.1002/asl.874.

Yang, X. L., and J. H. Sun, 2018: Organizational modes of severe wind-producing convective systems over North China. *Adv. Atmos. Sci.*, **35**, 540–549, https://doi.org/10.1007/s00376-017-7114-2.

——, ——, and Y. G. Zheng, 2017: A 5-yr climatology of severe convective wind events over China. *Wea. Forecasting*, **32**, 1289–1299, https://doi.org/10.1175/WAF-D-16-0101.1.

Zhang, W. L., and X. P. Cui, 2012: Main progress of torrential rain researches in North China during the past 50 years. *Torrential Rain Disaster*, **31**, 384–391.

Zheng, L. L., J. H. Sun, X. L. Zhang, and C. H. Liu, 2013: Organizational modes of mesoscale convective systems. *Wea. Forecasting*, **28**, 1081–1098, https://doi.org/10.1175/WAF-D-12-00088.1.

Zheng, Y. G., K. H. Zhou, J. Sheng, Y. J. Lin, F. Y. Tian, W. Y. Tang, Y. Lan, and W. J. Zhu, 2015: Advances in techniques of monitoring, forecasting and warning of severe convective weather. *J. Appl. Meteor. Sci.*, **26**, 641–657, https://doi.org/10.11898/1001-7313.20150601.